Redox Cycling in Individually Encapsulated Attoliter-Volume Nanopores

Seung-Ryong Kwon[a,*], Kaiyu Fu[b,*], Donghoon Han[c], and Paul W. Bohn[a,b,d]

[a]Department of Chemical and Biomolecular Engineering, University of Notre Dame, Notre Dame, Indiana 46556, United States
[b]Department of Chemistry and Biochemistry, University of Notre Dame, Notre Dame, Indiana 46556, United States
[c]Department of Chemistry, The Catholic University of Korea, Bucheon-si, Gyeonggi-do 14662, Republic of Korea
[d]Corresponding Author. Email *pbohn@nd.edu*

*Seung-Ryong Kwon and Kaiyu Fu contributed equally to this work.

Note: The authors declare no competing financial interest.

ABSTRACT

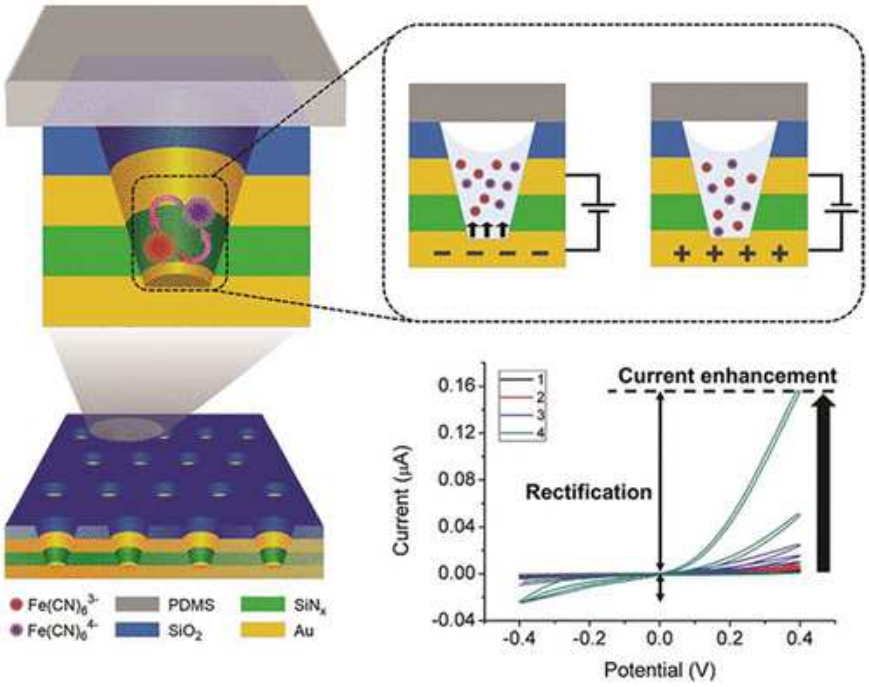

Redox cycling electrochemistry in arrays of individually encapsulated attoliter-volume ($V \sim 10$ aL) nanopores is investigated and reported here. These nanopore electrode array (NEA) structures exhibit distinctive electrochemical behaviors not observed in open NEAs, which allow free diffusion of redox couples between the nanopore interior and bulk solution. Confined nanopore environments, generated by sealing NEAs with a layer of poly(dimethylsiloxane), are characterized by enhanced currents—up to 250-fold compared with open NEAs—owing to effective trapping of the redox couple inside the nanopores and to enhanced mass transport effects. In addition, electrochemical rectification (*ca.* 1.5–6.3) was observed and is attributed to ion migration. Finite-element simulations were performed to characterize the concentration and electric potential gradients associated with the disk electrode, aqueous medium, and ring electrode inside the nanopores, and the results are consistent with experimental observations. The additional signal enhancement and redox-cycling-based rectification behaviors produced in these self-confined attoliter-volume nanopores are potentially useful in devising ultrasensitive sensors and molecular-based iontronic devices.

KEYWORDS

electric double layer; encapsulated nanopores; enhanced mass transport; ionic diode; redox cycling.

INTRODUCTION

In the past few decades, fabrication technologies have greatly advanced, making possible the evolution of electrochemical structures from micro- to nano- even to the sub-nanoscale, enabling the manufacture of highly efficient energy conversion/storage devices (*e.g.,* batteries,[1−3] super-capacitors,[4,5] and solar fuel cells[6,7]) as well as ultrasensitive bio/chemical sensors.[8−10] One common strategy to enhance the performance of electroanalytical methods is to reduce the size of the electrode, that is, ultra-microelectrodes, or nanoelectrodes, replacing conventional macroscale electrodes.[11,12] Besides enhanced mass transport, nanoelectrodes exhibit additional benefits arising from confined geometries that can constrain redox species in the vicinity of the electrode surface.[13−15] For example, thin-layer electrochemical cells, comprising parallel aligned electrodes with nanometer-scale gaps between them, have been employed in redox cycling paradigms where successive redox reactions across the nanogap amplify the output current. For example, Lemay and co-workers have determined fast electron-transfer kinetics based on rapid redox cycling of electrochemically active species traveling across a nanoscale gap between parallel electrodes.[16] Mirkin and co-workers have pushed this approach to its limit—successfully detecting characteristic electrochemical behavior of single molecules trapped in nanometer-wide thin-layer cells, providing information on mass transfer, electron-transfer kinetics, and double-layer effects.[17]

Understanding ion transport in relation to nanoscale electrodes is of particular importance in designing efficient energy conversion systems and electroanalytical platforms. At the macroscale, electrochemical measurements are generally carried out in the presence of supporting electrolyte (SE) to minimize solution resistance and screen electric fields.[18] On the other hand, if the distance between electrodes is <100 nm, electric double-layer (EDL) fields are a critical determinant of ion transport even at high SE concentrations owing to increasing size of the Debye length (λ_D) relative to the interelectrode distance.[19,20] Hence, the contribution of ion migration to the potential-derived mass transport should be carefully assessed. White and co-workers measured non-canonical steady-state peak-shaped voltammograms at low ionic strength, which was attributed to the effects of unscreened fields on ion transport,[21] and they also exploited the EDL field to enhance redox cycling.[22] In our laboratory, we demonstrated a strategy for faradaic signal amplification by exploiting the transport properties of ions inside densely packed arrays of nanopore-confined recessed ring-disk electrodes.[23,24] In the absence of supporting electrolyte, lowering the concentration of redox-active species (*e.g.,* $Ru(NH_3)_6^{3+}$ below 1 mM) increases the Debye length, λ_D, away from the charged pore surface, becoming comparable to the nanopore radius and leading to massive (200-fold) increases in faradaic current, which were determined to result from a combination of ion enrichment and migration effects.[24] Furthermore, by modifying the surface charge of the nanopores at low ionic strength, we were able to discriminate faradaic signals arising from redox-active species of different charges.[25]

An important limitation of these previous nanopore electrode array (NEA) experiments is that molecules could potentially escape the nanopore and be lost to the experiment. This is not problematic at large concentrations, but when the average pore occupancy drops near the single-molecule level (*i.e.,* $n_{pore} \sim 1$), then the impact on the experimental signal reaches a digitization threshold. To address this issue, here, we study the behavior of attoliter-volume-confined NEAs

with individual pore volumes of ~10 aL. In addition to highly efficient redox cycling, extra enhancement of faradaic currents arises from enhanced mass transport in the self-confined attoliter-volume nanopores. Finite-element simulations confirm the voltammogram response and provide detailed information regarding the spatial distribution of electric potential and concentration gradients inside the nanopores.

In addition to the useful mass transport effect, we also observe rectification. Previous studies of electrochemical rectification have employed multiple redox centers and/or modification of one electrode with a self-assembled monolayer (SAM) in order to achieve a nonlinear current response. For example, Mayer and co-workers devised a molecular transistor using interdigitated generator collector electrode arrays in which the collector was modified with a ferrocene-terminated SAM.[26] Similarly, Kwak and co-workers developed an electrochemical rectifier using a ferrocene-terminated SAM and soluble redox species incorporated into a thin-layer cell.[27] Recently, our laboratory reported asymmetric Nafion-coated NEAs as a redox-cycling-based diode.[28] Here, we demonstrate a strategy for rectifying electrochemical currents by manipulating ion migration without surface modification or multiple redox species. The rectified current response is dominated by contributions of ion migration, as confirmed by simulations, and the rectification ratio can be controlled by simply adjusting the ionic strength.

RESULTS AND DISCUSSION

Densely packed (5.5 pores μm^{-2}) NEAs were fabricated using a combination of nanosphere lithography (NSL) and reactive ion etching (Figures 1 and S1, Supporting Information (SI)). Silicon nitride (SiN_x, 100 nm) layers were interleaved between metal electrode layers to provide electrical insulation between the Au electrode layers, and SiO_2 (100 nm) was deposited on top to provide a hydrophilic surface and facilitate nanopore filling. The resulting NEAs exhibit significantly amplified currents, compared to single-electrode nanopores, due to rapid cycling of redox species between top and bottom electrodes in each nanopore.

Individually sealed attoliter-volume (13 aL) nanopores were fabricated into arrays in order to investigate the electrochemical behavior of redox species confined within the nanopores (Figure 1). After filling, a 5 mm thick poly(dimethylsiloxane) (PDMS) layer (*ca.* 1.5 × 1.5 cm^2) was placed over the NEA and gently pressed using a customized micrometer.[29] The PDMS capping layer confines redox species to the nanopore volume, with redox cycling reactions occurring between the nanometer-spaced internal electrodes. Once the NEAs were sealed by the PDMS cap, enhanced currents were observed in the two-electrode configuration, with enhancement increasing with scan number. Simultaneously, diode-like nonlinear current response was also observed when the experiments were carried out at low ionic strength. Below, we will demonstrate that these observations originate from ion migration coupled to enhanced mass transport.

Redox Cycling on Open NEAs.

To provide a basis for comparison, the electrochemical performance of NEAs was characterized employing both three- and four-electrode configurations as a function of redox species and supporting electrolyte concentrations with the pores open to the surrounding solution, allowing free exchange. Initially, 50 mM each of $K_3Fe(CN)_6$ and $K_4Fe(CN)_6$, was studied electrochemically in 2 M KNO_3. These experiments were conducted using either the bottom (disk) or top Au (ring) electrode (hereafter BE and TE, respectively) as the working

electrode (WE), whereas the other electrode was left at open-circuit potential. In this nongenerator collector (non-GC) mode, both BE and TE produced comparable current (∼1.8 μA), as expected based on their similar electrode areas (Figure S2). The calculated current in non-GC mode was 0.76 μA based on the equation for a recessed electrode:[30]

$$i = \frac{4\pi F C_b D a^2}{4L + \pi a} \quad (1)$$

where F is Faraday constant, C_b is the bulk concentration of $Fe(CN)_6^{3-}$ or $Fe(CN)_6^{4-}$ (50 mM), D is the diffusion coefficient (7.0×10^{-6} cm^2/s), a is the equivalent radius of the array of nanoelectrodes (56 μm), and L is the depth of the nanopores (300 nm). The difference between the experimental and calculated values may partially result from slightly overetched gold disk surfaces, leading to electrode areas larger than the geometric area.[24] Next, GC-mode, that is, redox cycling, experiments were implemented in the open-pore geometry by holding TE at +0.5 V and sweeping the potential of BE from +0.5 to −0.3 V vs Ag/AgCl. Under these conditions, $Fe(CN)_6^{3-}$ is reduced to $Fe(CN)_6^{4-}$ when E_{BE} approaches −0.3 V. $Fe(CN)_6^{4-}$ then diffuses to TE, where it is reoxidized to $Fe(CN)_6^{3-}$. Because the disk (BE) and ring (TE) electrodes are separated by only 100 nm, a significant enhancement in current, ∼39×, was achieved compared to operation in non-GC mode (Figure 2a). The simulated cyclic voltammograms (CVs) are in good agreement with experimental observations (cf. Figure 2b) when accounting for the ∼55 000 nanopores used to produce the experimental voltammograms, while 7 two-dimensional nanopores were employed in the simulations. Simulations also produced GC-mode currents enhanced by a factor of 24 over the non-GC result.

Next, we performed cyclic voltammetry on 100 mM $Fe(CN)_6^{3/4-}$ in the absence of SE. As shown in Figure 2c, a significant current enhancement, ∼30×, was also observed in the four-electrode configuration in comparison with non-GC mode, although the GC-mode enhancement was somewhat lower than that in 2 M KNO_3. Notably, $E^{0\prime}$ of $Fe(CN)_6^{3/4-}$ in the absence of SE shifts negative by ∼110 mV, implying that reduction of $Fe(CN)_6^{3-}$ in the absence of SE is less energetically favorable, which may be attributed to the requirement for counterions (K^+) to stabilize the highly charged state, thus resulting in the shift in $E^{0\prime}$ at low ionic strength.[31] Simulated CVs show a trend similar to that of the experimental results, with 22× current enhancement (Figure 2d).

When the concentration of $Fe(CN)_6^{3/4-}$ was further reduced to 10 mM in the absence of SE, $E^{0\prime}$ remained approximately the same (Figure 2e). However, both anodic and cathodic currents were inhibited, with GC mode/non-GC mode currents of 0.17 μA/0.062 μA, yielding a small (2.7×) redox-cycling-based enhancement. Extrapolating from the limiting current at 100 mM $Fe(CN)_6^{3/4-}$ in 2 M KNO_3 shown in Figure 2a, we would expect a GC-mode current of ∼6 μA. The suppressed redox cycling current is attributed principally to electrostatic repulsion between $Fe(CN)_6^{3/4-}$ and the charged electrodes. In addition, the electron-transfer rate constant is known to vary substantially with ionic strength.[32−34] Bond and co-workers demonstrated that the electrochemical behavior of $Fe(CN)_6^{3/4-}$ at low ionic strength is strongly affected by diffuse double-layer effects as posited here, that is, electrostatic interactions.[35]

In order to further illuminate these effects, we performed finite-element simulations for 10 mM $Fe(CN)_6^{3/4-}$ in the absence of SE using the same rate constant (k, 0.08 cm/s) used for simulation of 100 mM $Fe(CN)_6^{3/4-}$ in 2 M SE. The resulting simulations (Figure S3) show

electrochemical responses that are very different than the experimental observations (Figure 2e), as would be expected if the value of k was different at low ionic strength. In support of this hypothesis, simulations for k = 0.04 and 0.002 cm/s for 100 and 10 mM $Fe(CN)_6^{3/4-}$ in the absence of SE, respectively, produce simulated CVs (Figure 2f) that are similar to experimental results (Figure 2e), supporting the interpretation that the current at low ionic strength is affected by ion screening effects.

Redox Cycling on Open NEAs in Two-Electrode Configuration.

Next, we studied the electrochemical response of a NEAs in a two-electrode configuration using BE and TE as working and reference electrodes, respectively, without external reference or counter electrodes. Figure 3a shows that 100 mM $Fe(CN)_6^{3/4-}$ in 2 M KNO_3 exhibited about half of the GC current compared to the four-electrode configuration, that is, a 14× redox cycling enhancement. In addition, a slight asymmetry (25.0 and −23.5 μA for anodic and cathodic currents at ±0.4 V) in currents was observed. When concentrations of reduced and oxidized species (*e.g.*, 50 mM $Fe(CN)_6^{3-}$ and $Fe(CN)_6^{4-}$) are initially equal, the TE reference is expected to have *zero* overpotential if the response is Nernstian, and the ready accessibility of the TE to the bulk solutions should tend to hold the potential of TE near $E^{0\prime}$. Thus, the slightly asymmetric current response is likely due to electrostatic interactions of the redox species with BE and possibly natural convective flow caused by density differences between $K_3Fe(CN)_6$ and $K_4Fe(CN)_6$.[36]

Voltammetry of 100 mM $Fe(CN)_6^{3/4-}$ in the absence of SE was similar to that in the presence of 2 M KNO_3, albeit with a slight decrease in current in both potential directions and a small rectification (*i.e.,* $R = i_a/i_c$ = 1.3, Figure 3c). However, at 10 mM $Fe(CN)_6^{3/4-}$, the current decreased further, and R increased to 2.2 at ±0.4 V (Figure 3e), clearly indicating the influence of ion migration, particularly at low ionic strength. Simulated voltammograms produced rectification ratios R = 0.97, 1.15, and 1.49 at 100 mM $Fe(CN)_6^{3/4-}$ in 2 M KNO_3, 100 mM $Fe(CN)_6^{3/4-}$ without SE, and 10 mM $Fe(CN)_6^{3/4-}$ without SE, as shown in Figure 3b,d,f, respectively. As described above, the decrease in current largely arises from variation in k and rectification from diffuse double-layer effects, which were observed in the three-electrode configuration, just as in the three- and four-electrode configurations.

In the conventional four-electrode configuration described above, cyclic voltammetry was conducted with two working electrodes, including counter and *nonpolarizable* reference electrodes. The potentials applied to both working electrodes are precisely controlled relative to the reference electrode, so that the potential of the bulk solution potential is generally considered to be 0 V against the reference potential.[18] However, the two-electrode experiment just described uses two *polarizable* gold electrodes (BE and TE) without an external reference. Thus, the solution potential is not held at 0 V against the reference potential. Hence, it is important to specify the potential of the solution at the plane of electron transfer (PET), E_{sol}, while sweeping E_{BE} against E_{TE} because the potential difference of BE or TE with respect to solution at the PET determines the driving force for electron transfer. For example, the overpotential (η_{BE}) applied to BE is given by eq 2:[37]

$$\eta_{BE} = E_{BE} - E_{TE} - E_{sol} - E^{0\prime} \qquad (2)$$

where $E^{0\prime}$ is 0 V in the two Au electrode configuration due to equal concentrations of reduced and oxidized forms initially.

Finite-element simulations were performed to further characterize the open nanopore condition (Figure S4). As predicted, 100 mM $Fe(CN)_6^{3/4-}$ in 2 M KNO_3 (Figure S4b) exhibits solution potentials close to the E_{TE} reference potential (*i.e.,* 0 V), even at $E_{BE} = \pm 0.4$ V. In addition, the solution potential profiles are nearly constant from the PET of BE (0 nm) to TE (181 nm), indicating that the potential drop occurs almost entirely within the Helmholtz layer at BE (*i.e.,* 0.6 nm from the surface of BE). Thus, ion migration effects should be negligible for 100 mM $Fe(CN)_6^{3/4-}$ in 2 M KNO_3. In contrast, as the ionic strength is reduced, first to 100 mM $Fe(CN)_6^{3/4-}$ (Figure S4c) and then to 10 mM $Fe(CN)_6^{3/4-}$ (Figure S4d), both in the absence of SE, the solution potentials vary more strongly with E_{BE}. Therefore, both current rectification and the significantly suppressed current observed at lower ionic strength can be attributed to a combination of ion migration effects and sluggish electron-transfer kinetics.

Redox Cycling on Closed NEAs.

Physically segregating the internal volume of the nanopores by capping with PDMS dictates that all such experiments must be two-electrode experiments and are thus subject to the considerations discussed in the previous section. Surprisingly, we observed that, independent of initial concentration, as soon as the NEA was capped, the current began to increase with accumulated scans (Figure S5). Then once the current had reached the maximum value, it rapidly decreased, dropping eventually to a negligible current. It should be noted that higher viscosity solutions took longer to go through this cycle of increasing—then decreasing—current. In comparison to open NEAs (Figure 3a), an additional 6.8× increase in cathodic current was observed in capped NEAs (Figure 4a).

To explore the origin of the additional current enhancement in the closed NEAs, simulations were performed. As shown in Figure S6, simulations reveal only small current enhancements on closed, compared to open, NEAs. This small current enhancement is attributed to more efficient trapping of the redox species inside the self-confined nanopores. For comparison, redox cycling in the four-electrode configuration shown in Figure 2a produces currents that are substantially enhanced, indicating that redox cycling occurs at high efficiency, even though the redox species can freely diffuse in/out of open NEAs.

There are several possibilities that could give rise to the increasing, then decreasing, current. At long times, the collapse of the current is likely due to solution evaporation, which ultimately eliminates solution contact between BE and TE. There is precedent for considering evaporation from small confined volumes over time. For example, Walt and co-workers generated individual femtoliter reaction chambers with a PDMS capping layer, similar to the one used here, for their studies of single-enzyme activities and enzyme-linked bio-assays.[38] Their mechanical sealing method allowed reaction times typically up to 30 min limited by solution evaporation through the silicone. In the confined NEA system studied here, this would result in a current collapse when sufficient solution evaporates to eliminate the solution path between BE and TE, thereby bringing redox cycling to a halt.

Before the collapse, however, there is a clear and monotonic increase in the magnitude of the current with increasing scan number (time). Because the number of redox species confined to the pore does not change, and certainly does not increase with time, the changing current magnitude cannot result from a change in the number of redox-active species. This leaves only transport effects. Thus, we hypothesize an evaporation process that produces a spatially nonuniform liquid distribution (*e.g.,* a meniscus) that dramatically alters the nature of transport between BE and TE, enhancing the rates of electron transfer in the process.

Figure 4b shows CVs with 100 mM redox couple in the absence of SE on the closed NEAs. Analogous to the open NEAs shown in Figure 3c, a slightly rectified signal is observed, with R = 1.30, the same value obtained in open NEAs. When we compared the highest anodic current at E_{BE} = +0.4 V between the closed and open NEAs, a 7.9× enhancement was observed for closed NEAs. Interestingly, the anodic currents, *ca*. 170 μA in Figure 4a, are similar to or without SE, whereas the cathodic current at E_{BE} = −0.4 V is more inhibited in the absence of SE (*ca.* 120 μA in Figure 4b) than in the presence of SE (*ca.* 160 μA in Figure 4a). Again, this is likely due to electrostatic repulsions between the negatively charged redox species and BE. Accentuating this trend, Figure 4c shows a current that is enhanced by 135× in the closed NEAs compared to open NEAs (cf. Figure 3e) when the redox species concentration decreases from 100 to 10 mM.

In contrast, the rectification ratio R = 1.36 in the closed NEAs is somewhat smaller than the ratio, R = 2.2, in open NEAs. The smaller degree of rectification in the closed NEAs may arise from an increase in ionic strength inside the nanopores as the solution evaporates. Thus, the ion migration contribution to current is reduced, and the total current is predominantly governed by diffusion. Furthermore, the electron-transfer rate constant, k, also depends on ionic strength, increasing at higher ionic strength and leading to higher currents.

Manipulation of Rectified Redox Cycling Current.

Inspired by the nonlinear, rectified $i-V$ behavior at low ionic strength, we examined whether electrochemical rectification could be controlled by lowering the concentration of the redox couple. Three different 1 mM $Fe(CN)_6^{3/4-}$ solutions were prepared at 0, 0.01, and 2 M KNO_3. GC-mode current responses showed up to 24× enhancement with increasing SE concentration in the four-electrode configuration (Figure S7). Neither current enhancement based on redox cycling nor faradaic current in non-GC operation was observed in the absence of SE owing to sluggish electron-transfer kinetics at low ionic strength. Figure 5 shows voltammograms of 1 mM $Fe(CN)_6^{3/4-}$ obtained using the two-electrode configuration at 0, 0.01, and 2 M SE on both open and closed NEAs. Surprisingly, open NEAs exhibited very little response in the absence of SE (Figure 5a), presumably because at low ionic strength the negatively charged nanopore surfaces repel negative redox species, thereby reducing faradaic signals.[39] Given that λ_D for 1 mM $K_{3/4}Fe(CN)_6^{3/4-}$ without SE is estimated to be 3.4 nm, current might be affected by the surface charge to a small extent. However, it is more likely that the substantial decrease in current stems from the polarizability of the top Au reference electrode in the two-electrode configuration as well as alternating solution potential.

Once the NEAs are sealed with PDMS, the increasing-then-decreasing current behavior is observed, leaving only a small capacitive current (see Figure S8 for the case of 1 mM $Fe(CN)_6^{3/4-}$). However, although the overall magnitude of the current increases with increasing SE (cf. Figure 5d−f), the GC-mode enhancement and rectification ratio increase in the opposite sense, that is, with decreasing SE. Anodic current enhancements, 4×, 73×, and 250×, respectively, were obtained in closed NEAs as the ionic strength decreased from 2 to 0.01 to 0 M. At the highest current value shown in Figure 5d, a substantially amplified and rectified nonlinear $i-V$ response is exhibited with R = 6.3. The great enhancement (250-fold for anodic current) and strong electrochemical rectification arise from the ion migration and the mass transport effects that accompany solution evaporation from confined nanopores, as discussed above. As evidenced by the simulated CVs, when electrochemical analysis is performed using the two-electrode system, the solution potential tends more toward E_{TE} as ionic

strength increases. At 10 mM SE, faradaic signals from the open array increase slightly (Figure 5b), whereas the closed array exhibits a significant increase in current, 73×, and a rectification ratio, $R = 2.9$. When 2 M KNO_3 is used as SE with 1 mM $Fe(CN)_6^{3/4-}$, redox cycling current is recovered on the open NEAs (Figure 5c), and the closed NEA exhibits anodic current enhanced by 4× and a smaller rectification ratio, $R = 1.5$. Thus, the nonlinear, rectified $i-V$ responses present in nanometer-spaced nanopore electrode arrays can be successfully manipulated by controlling the migration effect through the SE concentration.

CONCLUSION

Here, we investigate cycling of redox species taking place in arrays of attoliter-volume individually encapsulated nanopores. The capped NEAs exhibit distinctive electrochemical phenomena, which are not observed in open nanopore arrays, where redox species can freely diffuse between one nanopore and the bulk solution or the adjacent nanopores. In the closed NEAs, additional current enhancement beyond that resulting from simple redox cycling, 4−250×, was achieved depending on ionic strength. In addition, we were able to manipulate the rectification ratio by controlling ion migration contributions to mass transport. Both the migration effect and variable electron-transfer kinetics influence the degree of electrochemical rectification and current in closed NEAs.

The additional current enhancement observed in physically capped nanopores suggests that current amplification beyond redox cycling may be useful for ultrasensitive chemical sensing. Furthermore, the successful manipulation of electrochemical rectification by means of ion migration is promising as a means of realizing molecule-based iontronic devices with actively controlled, that is, diode- or transistor-like electrical functionality. Typically, micro/nanofluidic diodes rely on asymmetric ion transport of inert electrolytes, for example, exploiting nonfaradaic current across charged conical nanopores.[40−42] However, the electrochemical rectification explored here is derived from direct faradaic reactions of redox species that undergo rapid redox cycling between electrodes with nanometer-scale separations, making highly amplified currents intrinsically accessible. Moreover, by taking advantage of nanopore structures presenting nanogap electrodes, current rectification can be controlled simply by varying ion migration effects without the need to modify the electrode surface. Thus, the present study on confined NEAs not only provides fundamental insights into nanoscale electrochemistry but also suggests applications in molecular iontronics and ultrasensitive sensors.

METHODS

Chemicals and Materials.

Potassium ferricyanide(III) ($K_3Fe(CN)_6$), potassium ferrocyanide(II) ($K_4Fe(CN)_6$), potassium nitrate (KNO_3), and polystyrene latex beads (0.46 μm in mean diameter) were purchased from Sigma-Aldrich (USA) and used as received. Poly(dimethylsiloxane) monomer and curing agent were obtained from Dow Corning (USA). All aqueous solutions were prepared using deionized water (18.2 MΩ cm, Millipore Milli-Q system) for electrochemical measurements.

Device Fabrication and Characterization.

NEAs were fabricated according to previously reported procedures from this laboratory.[39,43]

Briefly, the bottom and top electrodes of NEAs were patterned by metal deposition (UNIVEX 450B, Oerlikon), photolithography, and wet etching on precleaned glass slides (Glass D, Applied Microarrays, Inc.). An insulating layer of silicon nitride (SiN_x) between TE and BE as well as a passivation layer of SiO_2 on the top surface were deposited through plasma-enhanced chemical vapor deposition (PECVD 790, Plasma-Therm). Thereafter, a monolayer of polystyrene (PS) beads with an average diameter of 460 nm was formed at an air−liquid interface and then transferred to the glass slide by slow emersion through the interface. Subsequently, the size of PS beads was reduced to *ca.* 250 nm by a short O_2 plasma etch (Plasmatherm 790, 100 W). Next, a chromium-based nanoporous mask was deposited on the top of the glass slide, after which the PS beads were removed by immersion into chloroform or acetone. Afterward, a square pattern was defined by photolithography to limit the region (100 μm × 100 μm) of the NEAs to the intersection area of the bottom and top electrodes. Finally, NEAs were produced by transferring the pattern through the template using multistep reactive ion etching (Plasmatherm 790). During etching, each upper layer acts as the etch mask for the layer below it. For example, the Cr layer protects the SiO_2 layer, the SiO_2 protects the Au layer*, etc*. The scanning electron microscopy (SEM) images of NEAs were acquired by a FEI-Helios dual-beam focused ion beam at an accelerating voltage of 5 kV. Prior to imaging, all samples were sputter-coated with 2.5 nm iridium to avoid surface charging. The cross-sectional SEM images were acquired by depositing a protective Pt layer on the selected region of NEAs and gradually slicing the tilted sample with a focused ion beam.

Fabrication of Self-Encapsulated NEAs.
In order to create self-encapsulated NEAs, a roughly 5 mm thick PDMS layer was prepared from PDMS monomer and curing agent (10:1) and then cut into a small square piece with an area of *ca.* 1.5 × 1.5 cm^2. The square piece of PDMS layer was placed onto the surface of NEAs, which were prefilled with redox solution. Then, the PDMS layer was pressed gently against the NEA using a customized micrometer until the NEA device was completely closed. Electrochemical measurements were initiated immediately after mounting the confined NEAs.

Electrochemical Measurements.
All electrochemical measurements were conducted using a CHI842A electrochemical workstation (CH instruments, USA) in the presence of equal concentration of reduced ($Fe(CN)_6^{4-}$) and oxidized ($Fe(CN)_6^{3-}$) redox species. For non-GC mode operation, a three-electrode configuration was employed using either ring (TE) or disk (BE) gold (Au) as the working electrode, a platinum wire counter electrode, and a leak-free reference electrode (Harvard Apparatus, USA). For GC mode operation, both ring and disk Au electrodes were used as working electrodes with the platinum counter and the leak-free reference electrode in a four-electrode configuration. When the NEAs were capped by PDMS, the disk Au (BE) was used as working electrode, and the ring Au (TE) was used as a quasi-reference/counter electrode.

Simulation of Electrochemical Analysis.
Finite-element simulations were conducted using COMSOL Multiphysics (version 5.3) for redox cycling electrochemistry of $Fe(CN)_6^{3/4-}$ to predict potential and concentration profiles between the two gold electrodes inside nanopores. As the nanopore array consists of ∼5.5 × 10^4 pores on 100 × 100 μm^2, it was not possible to simulate the entire nanopore structure. Instead, two-dimensional geometry (1 × 1 mm^2) was used including seven nanopores, as shown in Figure S9.

The diffusion coefficients for $Fe(CN)_6^{3-}$, $Fe(CN)_6^{4-}$, K^+, and NO_3^- were set at 7.26×10^{-10}, 6.67×10^{-10}, 1.957×10^{-9}, and 1.902×10^{-9} m^2 s^{-1}, respectively.

The model employed in this study is similar to a previous report.[21] Typically, the "transport of diluted species" and "electrostatics" modules were employed in time-dependent mode. The Nernst−Planck equation was used to solve the mass transport of all species in the solution phase in the 2-D domain:

$$\frac{\partial c_i}{\partial t} = -D_i \nabla c_i - \frac{z_i F}{RT} D_i c_i \nabla \Phi \qquad (3)$$

where D_i, c_i, and z_i are the diffusion coefficient, the concentration, and the charge of the species i, respectively. F is Faraday's constant, and Φ is the electric potential. The left term indicates the diffusion flux, and the right term is associated with migrational flux. The covection flux was ignored in the simulation because all electrochemical measurements were performed in static solutions. The electric field was calculated using the Poisson equation

$$\nabla^2 \Phi = \frac{\rho}{\varepsilon_0 \varepsilon} \qquad (4)$$

where ε_0 is the vacuum permittivity and ε is the electrolyte dielectric constant; ρ is the space charge density calculated by the following equation:

$$\rho = F \sum_i z_i C_i \qquad (5)$$

The Butler−Volmer equation was used to determine electron-transfer kinetics

$$j_0 = k^0 c_R \exp\left[(1-\alpha)\frac{F}{RT}\left(E - E^{0\prime}\right)\right] - k^0 c_o \exp\left[-\alpha \frac{F}{RT}\left(E - E^{0\prime}\right)\right] \qquad (6)$$

where k^0 is the standard rate constant, $\alpha = 0.44$ is the transfer coefficient,[44] and E and $E^{0\prime}$ are the potentials applied to the electrode and the formal potential, respectively.

It is assumed that the plane of electron transfer occurs at 0.6 nm from the electrode surface, which is the thickness of the Helmholtz layers, and ε was set to be 6 within the Helmholtz layer and 80 for the bulk solution. The surface charge of SiO_2 and SiN_x layers was set to −1 mC/m^2.

ACKNOWLEDGMENTS

This work was supported by the National Science Foundation under Grant No. NSF1404744. K.F. was supported by an ACS Division of Analytical Chemistry graduate student fellowship, which was sponsored by Eastman Chemical Company. Structures used in these studies were fabricated in the Notre Dame Nanofabrication Facility and characterized in the Notre Dame Integrated Imaging Facility. The assistance of staff in both of these facilities is gratefully acknowledged.

REFERENCES

(1) Bruce, P. G.; Scrosati, B.; Tarascon, J. M. Nanomaterials for Rechargeable Lithium Batteries. *Angew. Chem., Int. Ed.* **2008**, 47, 2930−2946.
(2) Su, X.; Wu, Q.; Li, J.; Xiao, X.; Lott, A.; Lu, W.; Sheldon, B. W.; Wu, J. Silicon-Based Nanomaterials for Lithium-Ion Batteries: A Review. *Adv. Energy Mater*. **2014**, 4, 1300882.
(3) Sun, Y.; Liu, N.; Cui, Y. Promises and Challenges of Nanomaterials for Lithium-Based Rechargeable Batteries. *Nat. Energy* **2016**, 1, 16071.
(4) Yu, G.; Xie, X.; Pan, L.; Bao, Z.; Cui, Y. Hybrid Nanostructured Materials for High-Performance Electrochemical Capacitors. *Nano Energy* **2013**, 2, 213−234.
(5) Choi, H.; Yoon, H. Nanostructured Electrode Materials for Electrochemical Capacitor Applications. *Nanomaterials* **2015**, 5, 906−936.
(6) Yu, R.; Lin, Q.; Leung, S.-F.; Fan, Z. Nanomaterials and Nanostructures for Efficient Light Absorption and Photovoltaics. *Nano Energy* **2012**, 1, 57−72.
(7) Yu, M.; Long, Y.-Z.; Sun, B.; Fan, Z. Recent Advances in Solar Cells Based on One-Dimensional Nanostructure Arrays. *Nanoscale* **2012**, 4, 2783−2796.
(8) Arya, S. K.; Saha, S.; Ramirez-Vick, J. E.; Gupta, V.; Bhansali, S.; Singh, S. P. Recent Advances in ZnO Nanostructures and Thin Films for Biosensor Applications. *Anal. Chim. Acta* **2012**, 737, 1−21.
(9) Solanki, P. R.; Kaushik, A.; Agrawal, V. V.; Malhotra, B. D. Nanostructured Metal Oxide-Based Biosensors. *NPG Asia Mater*. **2011**, 3, 17.
(10) Zhu, C.; Yang, G.; Li, H.; Du, D.; Lin, Y. Electrochemical Sensors and Biosensors Based on Nanomaterials and Nanostructures. *Anal. Chem.* **2015**, 87, 230−249.
(11) Arrigan, D. W. J. A. Nanoelectrodes. *Analyst* **2004**, 129, 1157−1165.
(12) Henstridge, M. C.; Compton, R. G. J. T. C. R. Mass Transport to Micro-and Nanoelectrodes and Their Arrays. *A Review* **2012**, 12, 63−71.
(13) Gao, R.; Ying, Y. L.; Li, Y. J.; Hu, Y. X.; Yu, R. J.; Lin, Y.; Long, Y. T. A 30 nm Nanopore Electrode: Facile Fabrication and Direct Insights into the Intrinsic Feature of Single Nanoparticle Collisions. *Angew. Chem., Int. Ed*. **2018**, 57, 1011−1015.
(14) Ying, Y.-L.; Hu, Y.-X.; Gao, R.; Yu, R.-J.; Gu, Z.; Lee, L. P.; Long, Y.-T. Asymmetric Nanopore Electrode-Based Amplification for Electron Transfer Imaging in Live Cells. *J. Am. Chem. Soc.* **2018**, 140, 5385−5392.
(15) Yu, R.-J.; Ying, Y.-L.; Gao, R.; Long, Y.-T. Confined Nanopipette Sensing: From Single Molecules, Single Nanoparticles to Single Cells. *Angew. Chem., Int. Ed.* **2018**, DOI: 10.1002/ anie.201803229.
(16) Zevenbergen, M. A.; Wolfrum, B. L.; Goluch, E. D.; Singh, P. S.; Lemay, S. G. Fast Electron-Transfer Kinetics Probed in Nanofluidic Channels. *J. Am. Chem. Soc*. **2009**, 131, 11471−11477.
(17) Sun, P.; Mirkin, M. V. Electrochemistry of Individual Molecules in Zeptoliter Volumes. *J. Am. Chem. Soc*. **2008**, 130, 8241−8250.
(18) Bard, A. J.; Faulkner, L. R. *Electrochemical Methods: Fundamentals and Applications*, 2nd ed.; John Wiley & Sons: New York, 2001.
(19) Fan, L.; Liu, Y.; Xiong, J.; White, H. S.; Chen, S. Electron-Transfer Kinetics and Electric Double Layer Effects in Nanometer-Wide Thin-Layer Cells. *ACS Nano* **2014**, 8, 10426−10436.
(20) Lu, J.; Zhang, B. Electrostatic Ion Enrichment in an Ultrathin-Layer Cell with a Critical Dimension between 5 and 20 nm. *Anal. Chem*. **2017**, 89, 2739−2746.

(21) Xiong, J.; Chen, Q.; Edwards, M. A.; White, H. S. Ion Transport within High Electric Fields in Nanogap Electrochemical Cells. *ACS Nano* **2015**, 9, 8520−8529.
(22) Chen, Q.; McKelvey, K.; Edwards, M. A.; White, H. S. Redox Cycling in Nanogap Electrochemical Cells. The Role of Electrostatics in Determining the Cell Response. *J. Phys. Chem. C* **2016**, 120, 17251−17260.
(23) Ma, C.; Contento, N. M.; Gibson, L. R.; Bohn, P. W. Redox Cycling in Nanoscale-Recessed Ring-Disk Electrode Arrays for Enhanced Electrochemical Sensitivity. *ACS Nano* **2013**, 7, 5483−5490.
(24) Ma, C.; Contento, N. M.; Bohn, P. W. Redox Cycling on Recessed Ring-Disk Nanoelectrode Arrays in the Absence of Supporting Electrolyte. *J. Am. Chem. Soc*. **2014**, 136, 7225−7228.
(25) Fu, K.; Bohn, P. W. Nanochannel Arrays for Molecular Sieving and Electrochemical Analysis by Nanosphere Lithography Templated Graphoepitaxy of Block Copolymers. *ACS Appl. Mater. Interfaces* **2017**, 9, 24908−24916.
(26) Liu, Y.; Wolfrum, B.; Hüske, M.; Offenhausser, A.; Wang, E.; Mayer, D. Transistor Functions Based on Electrochemical Rectification. *Angew. Chem., Int. Ed*. **2013**, 52, 4029−4032.
(27) Park, S.; Park, J. H.; Hwang, S.; Kwak, J. Programmable Electrochemical Rectifier Based on a Thin-Layer Cell. *ACS Appl. Mater. Interfaces* **2017**, 9, 20955−20962.
(28) Fu, K.; Han, D.; Kwon, S.-R.; Bohn, P. W. Asymmetric Nafion-Coated Nanopore Electrode Arrays as Redox-Cycling-Based Electrochemical Diodes. *ACS Nano* **2018**, 12, 9177−9185.
(29) Rissin, D. M.; Walt, D. R. Digital Concentration Readout of Single Enzyme Molecules Using Femtoliter Arrays and Poisson Statistics. *Nano Lett.* **2006**, 6, 520−523.
(30) Bond, A. M.; Luscombe, D.; Oldham, K. B.; Zoski, C. G. A Comparison of the Chronoamperometric Response at Inlaid and Recessed Disc Microelectrodes. *J. Electroanal. Chem. Interfacial Electrochem.* **1988**, 249, 1−14.
(31) Tran, E.; Cohen, A. E.; Murray, R. W.; Rampi, M. A.; Whitesides, G. M. Redox Site-Mediated Charge Transport in a Hg−SAM//$Ru(NH_3)_6^{3+/2+}$//SAM−Hg Junction with a Dynamic Inter-electrode Separation: Compatibility with Redox Cycling and Electron Hopping Mechanisms. *J. Am. Chem. Soc.* **2009**, 131, 2141−2150.
(32) Beriet, C.; Pletcher, D. A Microelectrode Study of the Mechanism and Kinetics of the Ferro/Ferricyanide Couple in Aqueous Media: The Influence of the Electrolyte and Its Concentration. *J. Electroanal. Chem.* **1993**, 361, 93−101.
(33) Tsierkezos, N. G.; Ritter, U. Influence of Concentration of Supporting Electrolyte on Electrochemistry of Redox Systems on Multi-Walled Carbon Nanotubes. *Phys. Chem. Liq*. **2012**, 50, 661−668.
(34) Kůta, J.; Yeager, E. The Influence of Cations on the Electrode Kinetics of Ferricyanide-Ferrocyanide System on the Rotating Gold Electrode. *J. Electroanal. Chem. Interfacial Electrochem.* **1975**, 59, 110−112.
(35) Rooney, M. B.; Coomber, D. C.; Bond, A. M. Achievement of Near-Reversible Behavior for the $[Fe(CN)_6]^{3-/4-}$ Redox Couple Using Cyclic Voltammetry at Glassy Carbon, Gold, and Platinum Macrodisk Electrodes in the Absence of Added Supporting Electrolyte. *Anal. Chem*. **2000**, 72, 3486−3491.
(36) Gao, X.; Lee, J.; White, H. S. Natural Convection at Microelectrodes. *Anal. Chem*. **1995**, 67, 1541−1545.
(37) Sarkar, S.; Mathwig, K.; Kang, S.; Nieuwenhuis, A. F.; Lemay, S. G. Redox Cycling without Reference Electrodes. *Analyst* **2014**, 139, 6052−6057.

(38) Mogalisetti, P.; Walt, D. R. Enzyme Kinetics in Femtoliter Arrays. *Methods Enzymol.* **2016**, 581, 541−560.
(39) Fu, K.; Han, D.; Ma, C.; Bohn, P. W. Ion Selective Redox Cycling in Zero-Dimensional Nanopore Electrode Arrays at Low Ionic Strength. *Nanoscale* **2017**, 9, 5164−5171.
(40) Yameen, B.; Ali, M.; Neumann, R.; Ensinger, W.; Knoll, W.; Azzaroni, O. Single Conical Nanopores Displaying pH-Tunable Rectifying Characteristics. Manipulating Ionic Transport with Zwitterionic Polymer Brushes. *J. Am. Chem. Soc*. **2009**, 131, 2070−2071.
(41) Wang, D.; Kvetny, M.; Liu, J.; Brown, W.; Li, Y.; Wang, G. Transmembrane Potential across Single Conical Nanopores and Resulting Memristive and Memcapacitive Ion Transport. *J. Am. Chem. Soc*. **2012**, 134, 3651−3654.
(42) Yan, R.; Liang, W.; Fan, R.; Yang, P. Nanofluidic Diodes Based on Nanotube Heterojunctions. *Nano Lett*. **2009**, 9, 3820−3825.
(43) Fu, K.; Han, D.; Ma, C.; Bohn, P. W. Electrochemistry at Single Molecule Occupancy in Nanopore-Confined Recessed Ring-Disk Electrode Arrays. *Faraday Discuss*. **2016**, 193, 51−64.
(44) Bae, J. H.; Yu, Y.; Mirkin, M. V. Diffuse Layer Effect on Electron-Transfer Kinetics Measured by Scanning Electrochemical Microscopy (SECM). *J. Phys. Chem. Lett*. **2017**, 8, 1338−1342.

FIGURES

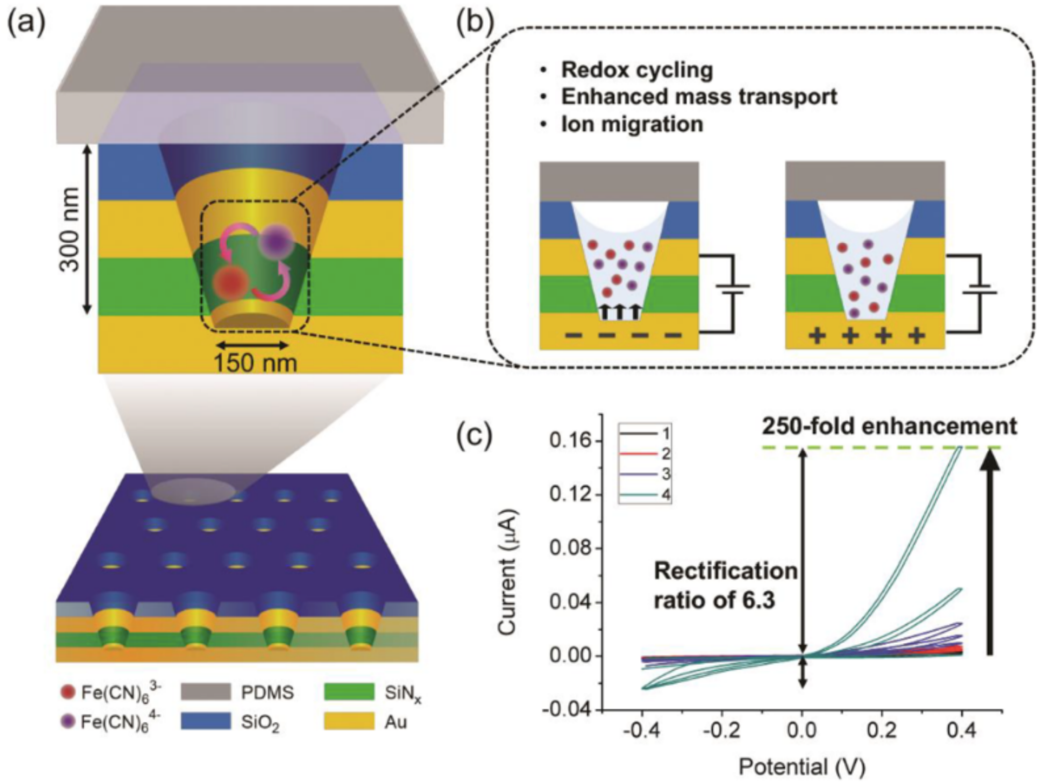

Figure 1. (a) Schematic illustration of attoliter-volume-confined NEAs sealed with a poly(dimethylsiloxane) capping layer. (b) Representative ion distributions altered by the polarity of the bottom (working) *vs* top (reference) electrode. (c) Simultaneous current enhancement and rectification with increasing number of potential scans reflect ion migration and enhanced mass transport inside the NEAs. The left and right schemes of panel (b) depict the situation at negative and positive potentials in panel (c), respectively.

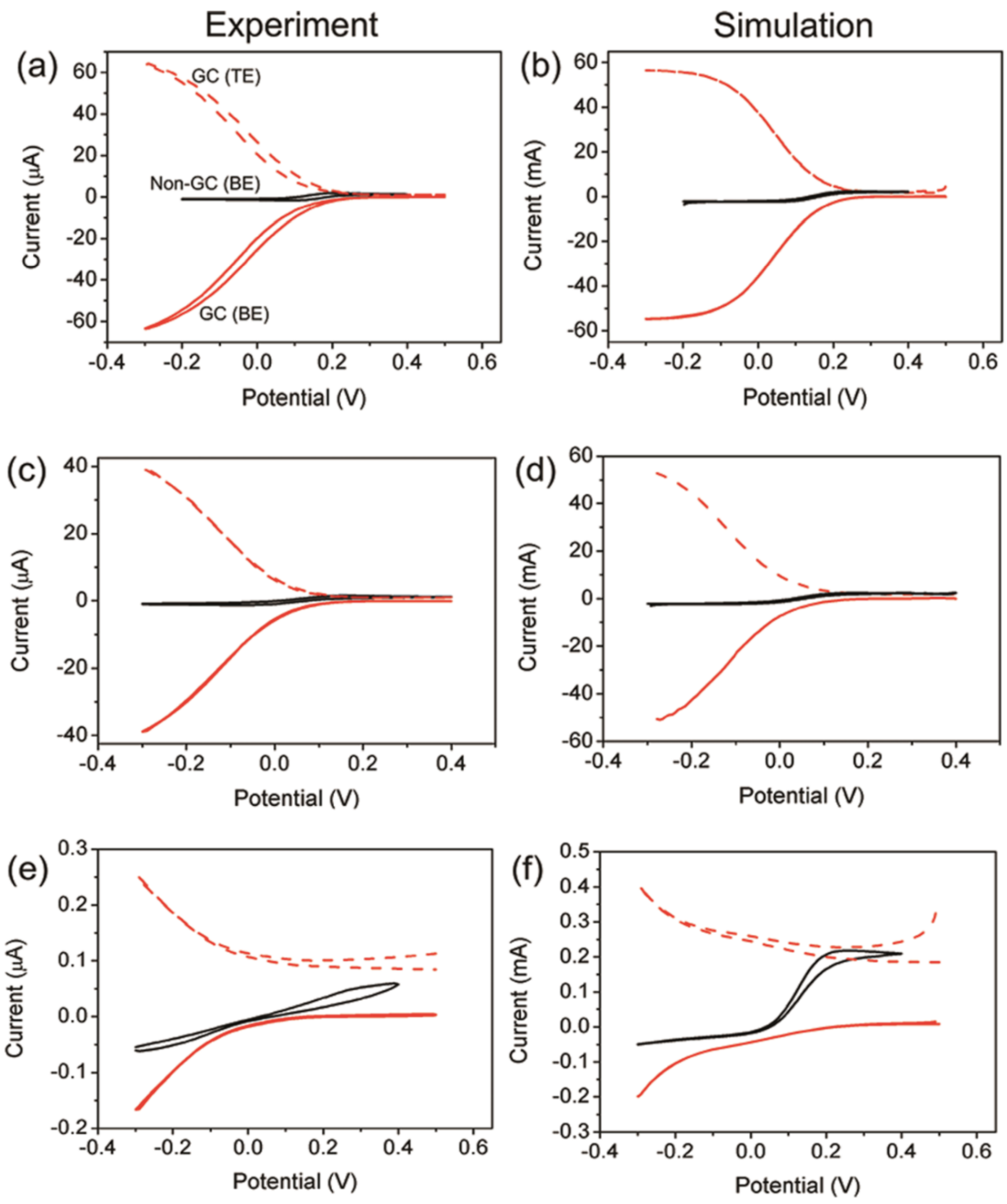

Figure 2. Experimental (a,c,e) and simulated (b,d,f) voltammograms of 100 mM $Fe(CN)_6^{3/4-}$. (a,b) Electrolyte is 100 mM $Fe(CN)_6^{3/4-}$ + 2 M KNO_3 ; (c,d) 100 mM $Fe(CN)_6^{3/4-}$ only, *i.e.*, no other SE; and (e,f) 10 mM $Fe(CN)_6^{3/4-}$ only. Black: non-GC mode operation, in which BE was used as working electrode and TE was left at open-circuit potential (three-electrode system). Red: GC-mode, in which both BE (solid line) and TE (dashed line) were employed as working electrodes (four-electrode system); TE was held at ~0.45 V for oxidation of $Fe(CN)_6^{3/4-}$, and the potential of BE was swept at a scan rate of 0.1 V s^{-1}. Rate constants I = 0.08 (b), 0.04 (d), and 0.002 (f) cm/s were used to obtain the simulated voltammograms.

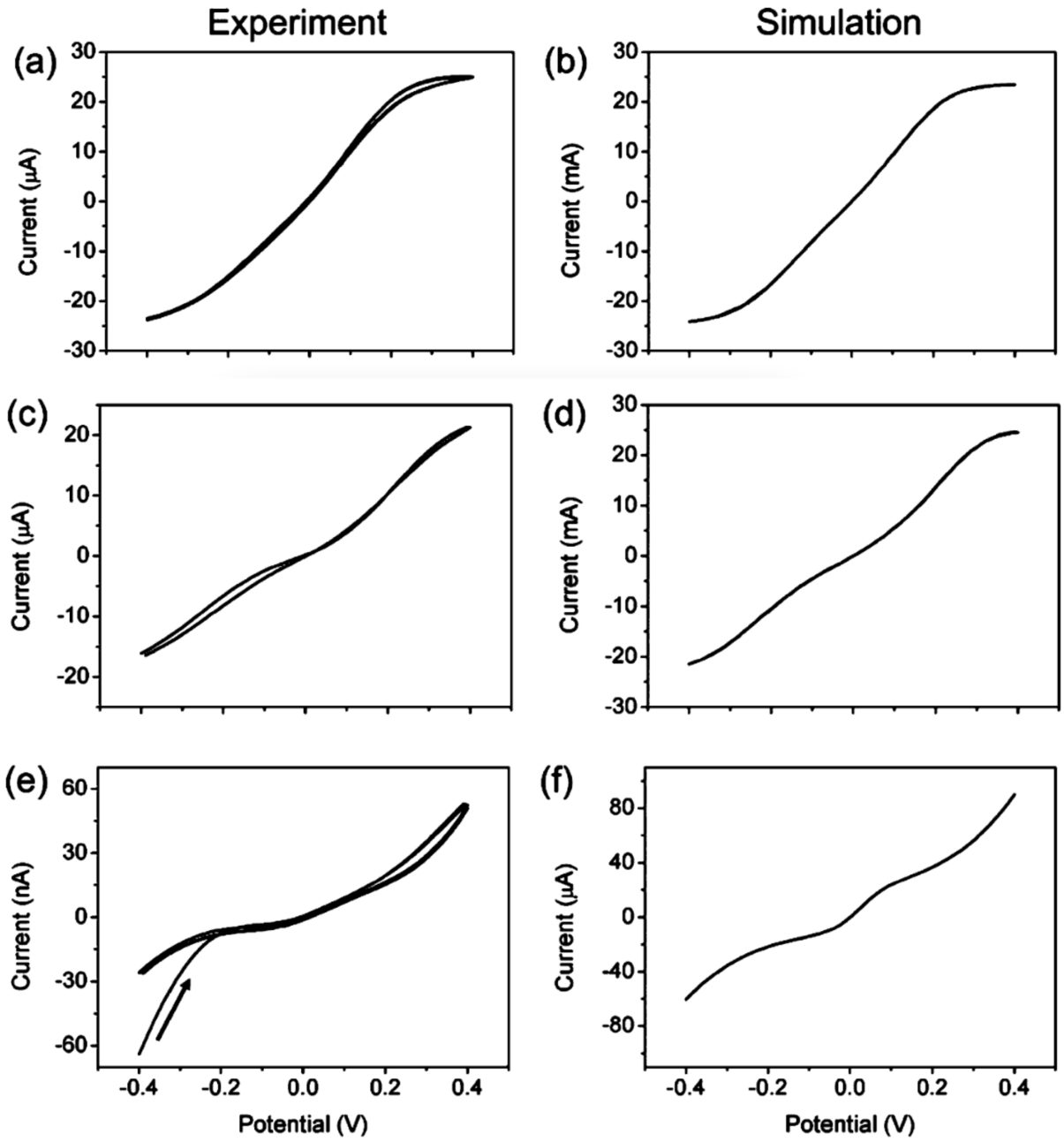

Figure 3. Experimental (a,c,e) and simulated (b,d,f) voltammograms on open NEAs obtained using BE as working and TE as reference electrode without external reference or counter electrodes: (a,b) 100 mM $Fe(CN)_6^{3/4-}$ in 2 M KNO_3 ; (c,d) 100 mM $Fe(CN)_6^{3/4-}$ with no SE; (e,f) 10 mM $Fe(CN)_6^{3/4-}$ with no SE. Scan rate was 0.1 V s^{-1} .

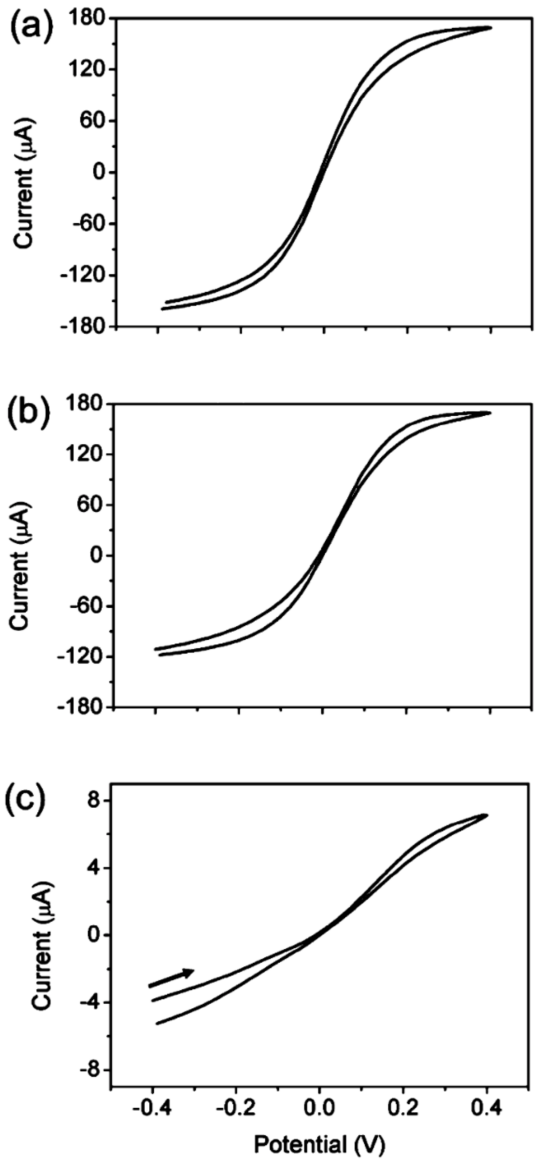

Figure 4. Experimental voltammetric responses of (a) 100 mM $Fe(CN)_6^{3/4-}$ in 2 M KNO_3; (b) 100 mM $Fe(CN)_6^{3/4-}$ in the absence of SE; and (c) 10 mM $Fe(CN)_6^{3/4-}$ in the absence of SE. All measurements were performed in closed arrays with a PDMS cladding layer, and only the maximum current response is shown; see Figure S5 for the full sequence of voltammograms. In all experiments, BE and TE were used as working and reference electrodes in a two-electrode configuration, and the scan rate was 0.1 V s^{-1}.

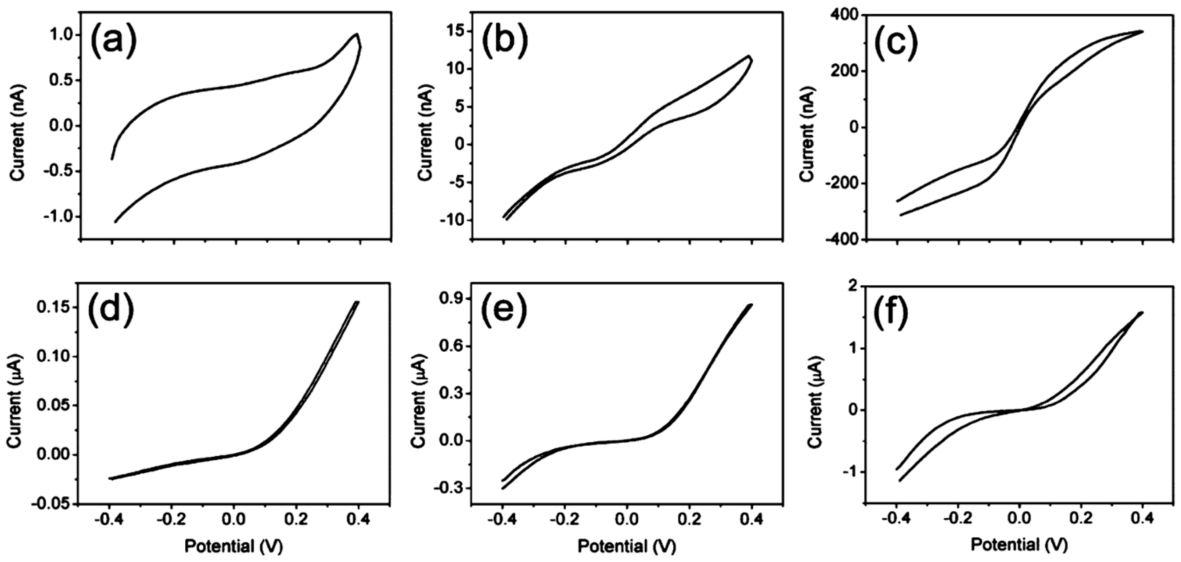

Figure 5. Voltammetric responses of 1 mM $Fe(CN)_6^{3/4-}$ in (a,d) 0; (b,e) 0.01 M; and (c,f) 2 M KNO_3 using the two-electrode configuration in either open (a−c) or closed (d−f) NEAs. Only maximum current responses are displayed for the closed arrays. The scan rate was 0.1 V s^{-1}.

Supporting Information

Redox Cycling in Individually-Encapsulated Attoliter-Volume Nanopores

Seung-Ryong Kwon[1,§], Kaiyu Fu[2,§], Donghoon Han[3], and Paul W. Bohn[1,2*]

[1]Department of Chemical and Biomolecular Engineering, University of Notre Dame, Notre Dame, IN 46556

[2]Department of Chemistry and Biochemistry, University of Notre Dame, Notre Dame, IN 46556

[3]Department of Chemistry, The Catholic University of Korea, Bucheon-si, Gyeonggi-do, 14662, Republic of Korea

[§]These authors equally contributed to this work.

[*]Author to whom correspondence should be addressed, *pbohn@nd.edu*

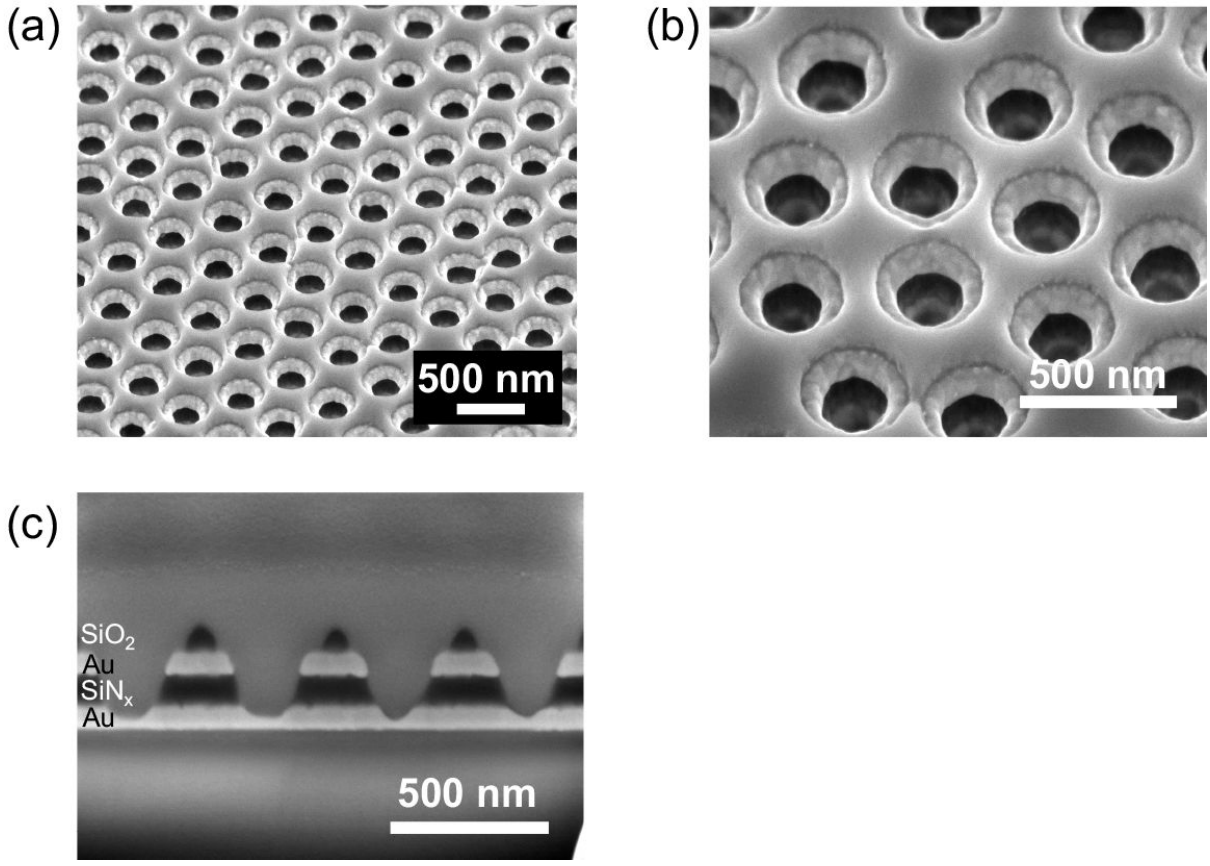

Figure S1. (a) SEM image of nanopore electrode arrays (NEAs) at 52° tilt; (b) an expanded view of the NEAs at 35° tilt. (c) Cross-sectional SEM image of the array showing the vertical layered structure of the nanopores.

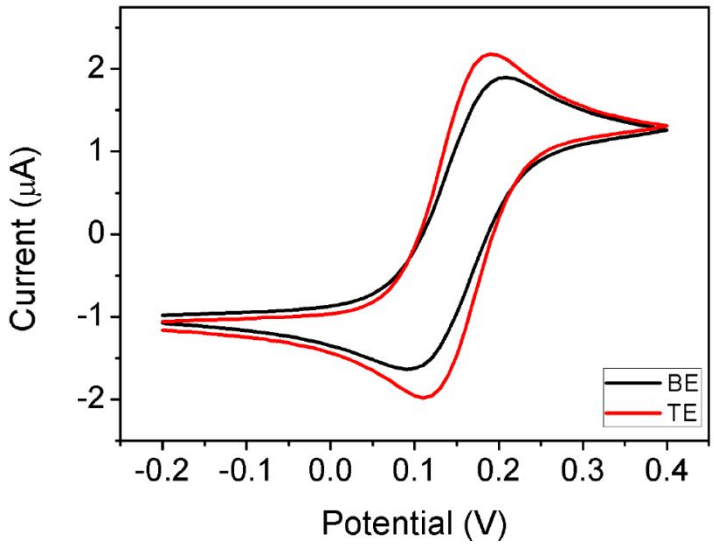

Figure S2. Non-GC mode voltammograms of 100 mM $Fe(CN)_6^{3/4-}$ in 2 M KNO_3 in the open pore configuration. Either BE (black) or TE (red) was used as the working electrode in a three-electrode configuration (Pt wire counter, Ag/AgCl reference). Potential was swept at 0.1 V s^{-1}.

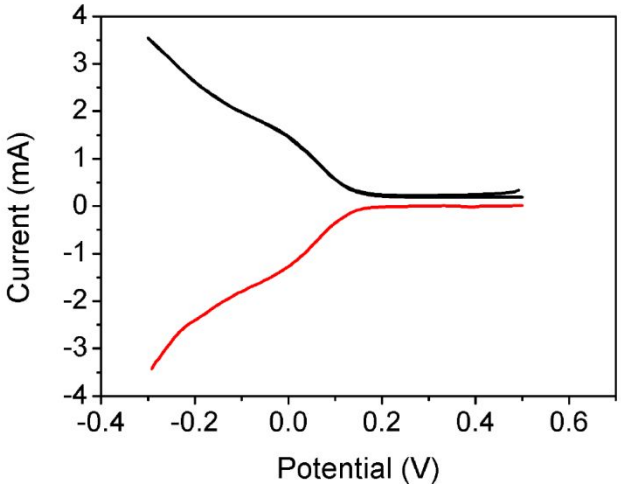

Figure S3. Simulated CVs of 10 mM $Fe(CN)_6^{3/4-}$ in the absence of SE using a rate constant, 0.08 cm/s, appropriate for 2 M KNO_3. TE (black curve) was held at +0.5 V, while E_{BE} (red) was swept between +0.5 and –0.3 V vs. Ag/AgCl at 0.1 V s^{-1}.

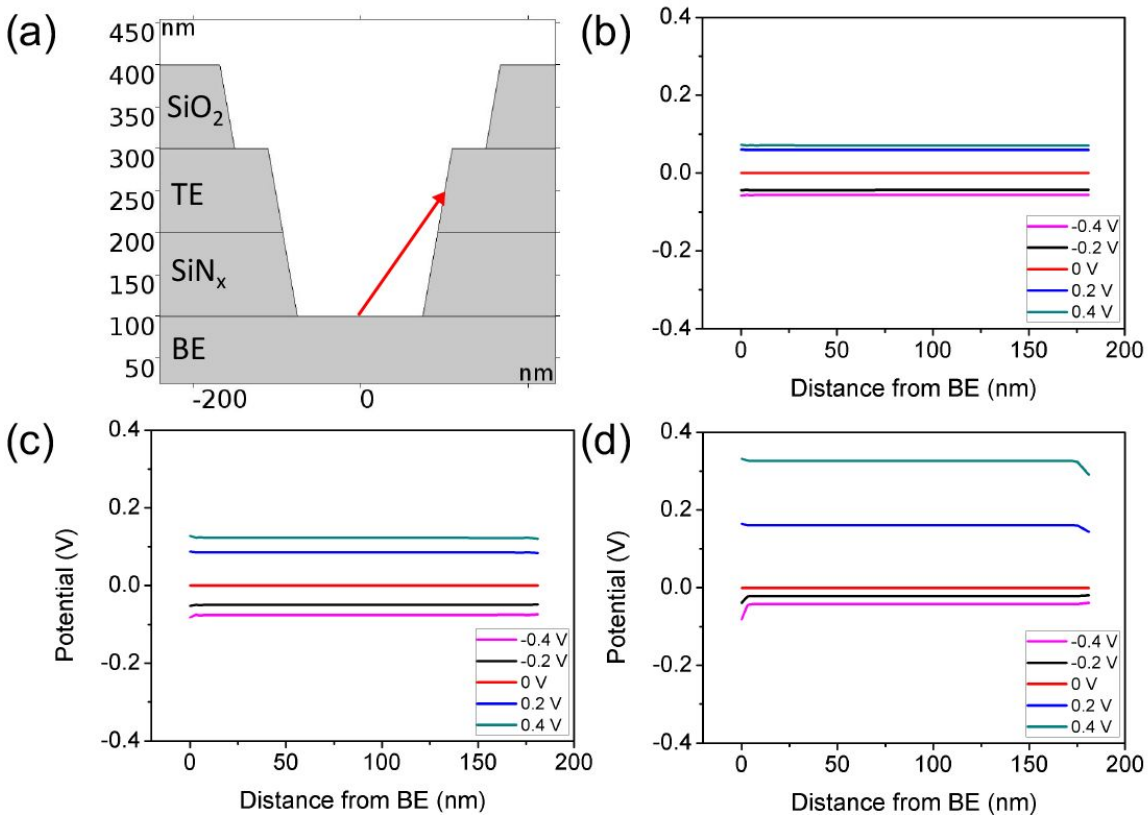

Figure S4. Simulated potential profiles from the plane of electron transfer at BE, *i.e.* 0.6 nm from the electrode surface, to that at TE along with the red line in (a). Inset legends indicate the potential applied to BE relative to TE, *i.e.* 0 V *vs*. the external circuit potential. (b) 100 mM $Fe(CN)_6^{3/4-}$ in 2 M KNO_3; (c) 100 mM $Fe(CN)_6^{3/4-}$ in the absence of SE; (d) 10 mM $Fe(CN)_6^{3/4-}$ in the absence of SE.

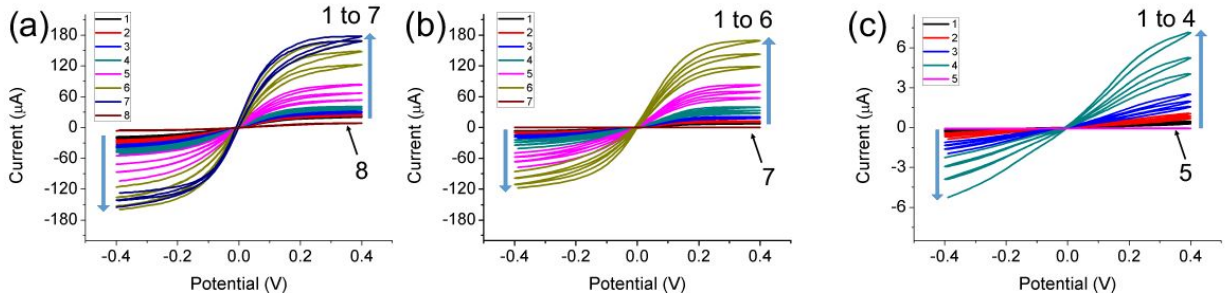

Figure S5. Consecutive voltammograms obtained from: (a) 100 mM $Fe(CN)_6^{3/4-}$ in 2 M KNO_3; (b) 100 mM $Fe(CN)_6^{3/4-}$ in the absence of SE; and (c) 10 mM $Fe(CN)_6^{3/4-}$ in the absence of SE. The numbers denote the order in which the CVs were obtained, with the last number in each panel indicating a voltammogram obtained after the current response was lost. Each voltammetric set consists of 4~6 potential cycles. The scan rate was 0.1 V s^{-1}.

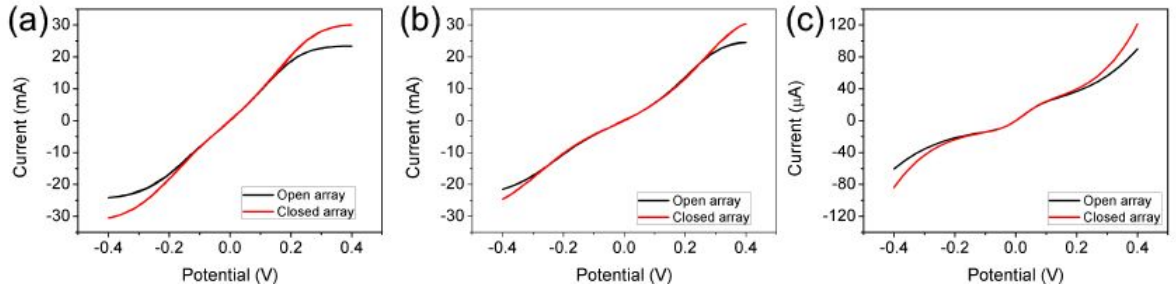

Figure S6. Simulated voltammograms of: (a) 100 mM $Fe(CN)_6^{3/4-}$ in 2 M KNO_3; (b) 100 mM $Fe(CN)_6^{3/4-}$ in the absence of SE; and (c) 10 mM $Fe(CN)_6^{3/4-}$ in the absence of SE. Black and red curves were obtained in open and closed pore geometries, respectively.

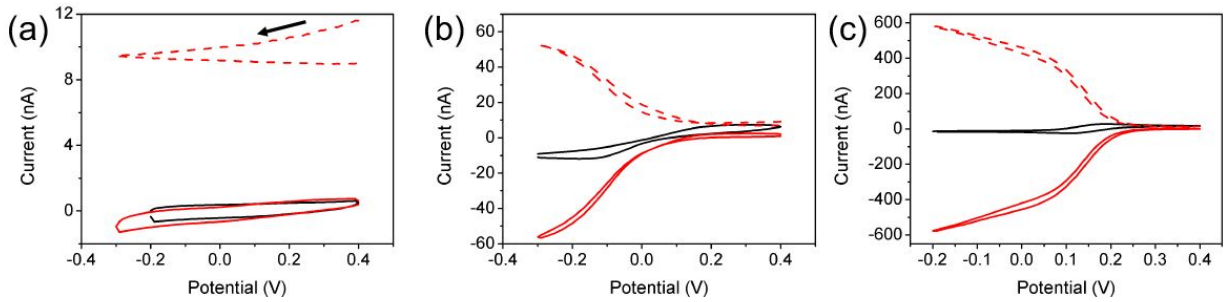

Figure S7. Experimental voltammograms of 1 mM $Fe(CN)_6^{3/4-}$ with: (a) 0 M; (b) 0.01 M; and (c) 2 M KNO_3. Black curves result from non-GC operation, in which BE is the working electrode in a 3-electrode configuration. Red curves denote GC mode operation using both BE and TE as working electrodes in a 4-electrode configuration (straight line: BE, dashed line: TE); TE was held at +0.4 V while the potential of BE was swept at a scan rate of 0.1 V s^{-1}.

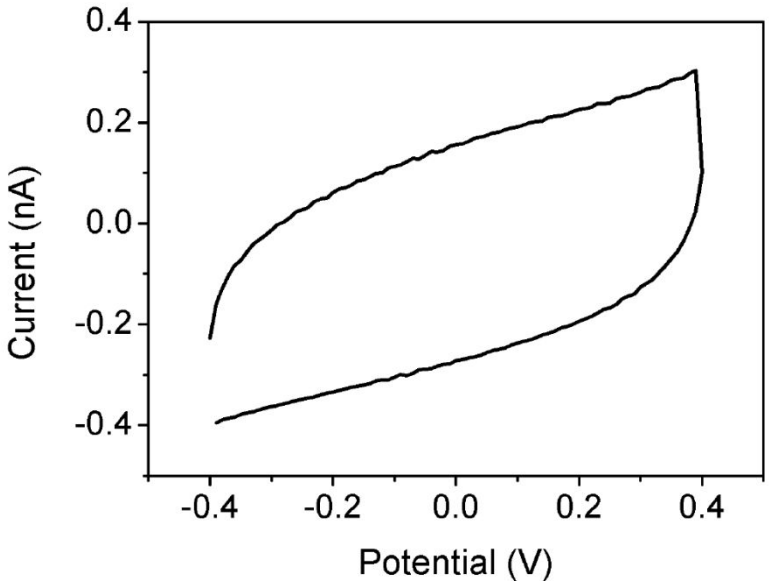

Figure S8. Voltammogram of 1 mM $Fe(CN)_6^{3/4-}$ in the absence of SE showing capacitive response after the solution in the sealed nanopore array evaporates.

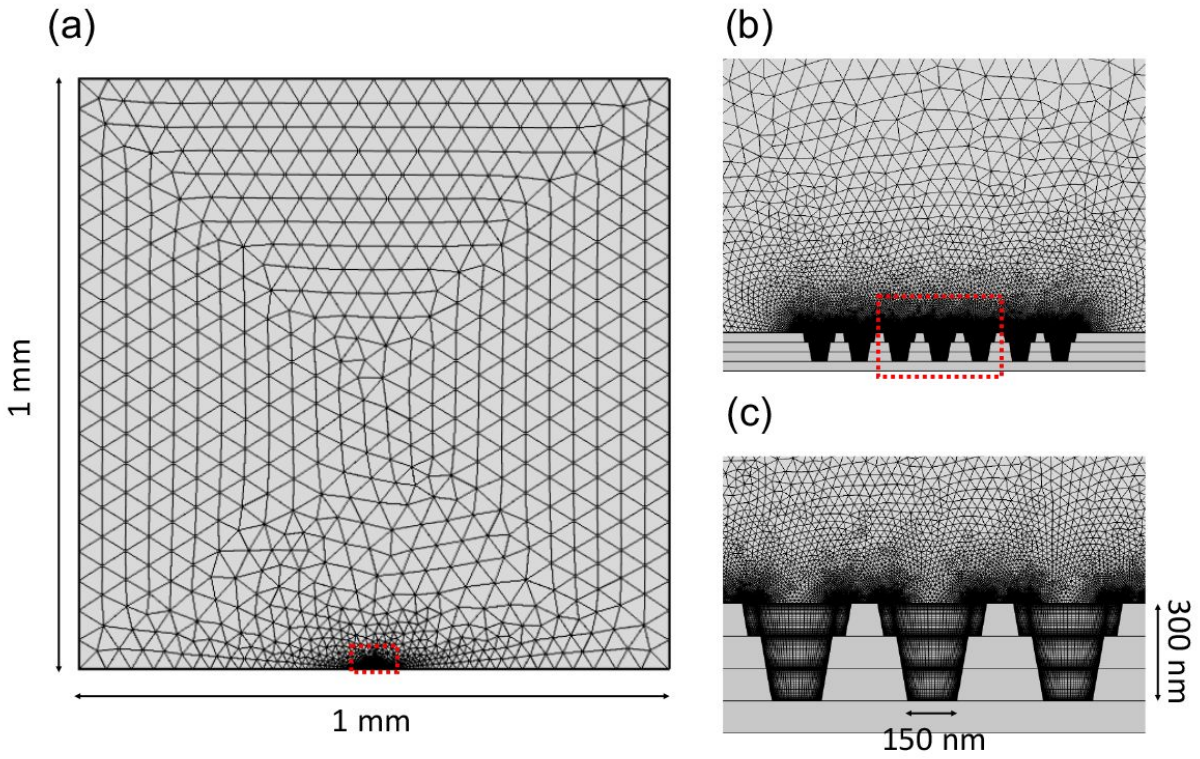

Figure S9. Mesh formation used for the finite simulations showing the whole 2D geometry (a) and enlarged images including nanopore structures (b, c).